Multiwalled nanotube faceting unravelled

Itai Leven[1†], Roberto Guerra[2,3†], Andrea Vanossi[2,3], Erio Tosatti[2,3,4] and Oded Hod[1*]

Nanotubes show great promise for miniaturizing advanced technologies. Their exceptional physical properties are intimately related to their morphological and crystal structure. Circumferential faceting of multiwalled nanotubes reinforces their mechanical strength and alters their tribological and electronic properties. Here, the nature of this important phenomenon is fully rationalized in terms of interlayer registry patterns. Regardless of the nanotube identity (that is, diameter, chirality, chemical composition), faceting requires the matching of the chiral angles of adjacent layers. Above a critical diameter that corresponds well with experimental results, achiral multiwalled nanotubes display evenly spaced extended axial facets whose number equals the interlayer difference in circumferential unit cells. Elongated helical facets, commonly observed in experiment, appear in nanotubes that exhibit small interlayer chiral angle mismatch. When the wall chiralities are uncorrelated, faceting is suppressed and outer layer corrugation, which is induced by the Moiré superlattice, is obtained in agreement with experiments. Finally, we offer an explanation for the higher incidence of faceting in multiwalled boron nitride nanotubes with respect to their carbon-based counterparts.

As their name suggests, nanotubes are traditionally thought of as cylindrical structures that possess a circular cross-section. Nevertheless, under certain conditions multiwalled nanotubes (MWNTs) exhibit circumferential faceting, which results in polygonal cross-sections[1–8]. This, in turn, leads to considerable reinforcement of their mechanical properties[7,9] thus paving the way for fulfilling their potential as next-generation ultrahigh-strength materials[10–12]. Furthermore, it may have considerable impact on their tribological, electronic and optical properties. A thorough understanding of the nature and origin of this phenomenon is thus crucial for the rational design of robust and durable nanotube-based electromechanical devices that can withstand repeated mechanical loads.

The underlying mechanism for nanotube faceting clearly involves a balance between the interlayer attractive interactions that are gained at the faceted regions and the mechanical strain accumulated at the vertices. This understanding has been the basis for several theoretical studies that adopted the continuum model approach[13–16]. Such models provide valuable insights regarding the general phenomenon; however, they are limited in their ability to depict important system-specific characteristics that require a detailed atomistic description. This was clearly demonstrated when a fully atomistic dispersion-corrected anisotropic tight-binding Hamiltonian model for graphitic systems was used to investigate pentagonal faceting in nested multiwalled zigzag nanotubes[17]. Nevertheless, many important questions remain, including: what are the detailed conditions required for faceting to occur? What dictates the number of facets formed? And why is this phenomenon more commonly observed in multiwalled boron nitride nanotubes (MWBNNTs) than in their carbon-based counterparts?

In the present study we identify the atomistic origin of nanotube faceting as resulting from extended interlayer registry patterns that appear between the curved hexagonal lattices that form the nanotube walls. We find that when two adjacent walls have matching chiral angles, their curvature difference forms localized out-of-registry regions that are evenly spaced along the circumference of the tube and are separated by extended in-registry arcs. Upon
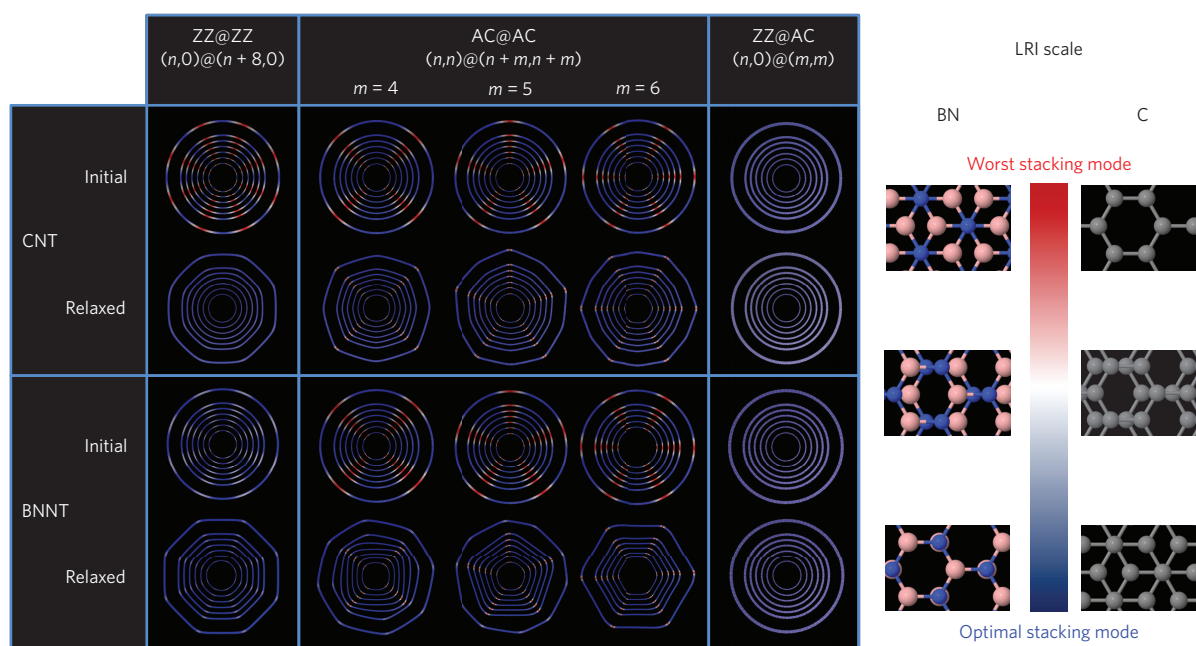
structural relaxation the former become vertices whereas the latter form commensurate facets. Interestingly, the number of facets is dictated by the difference in the circumferential unit cells between two adjacent layers. Furthermore, the facets can be either axial or helical depending on the chiral angle difference of adjacent layers. Finally, the critical tube diameter above which faceting is found lies between 5 and 13 nm depending on the tube chirality, in good agreement with experimental observations[7]. On the basis of these findings we offer an explanation for the relative abundance of faceting in inorganic nanotubes with respect to their graphitic counterparts.

Achiral double-walled nanotubes

Let us first discuss achiral double-walled nanotubes (DWNTs). Four different types of DWNT system exist, where the inner and outer layers can be either zigzag (ZZ) or armchair (AC). In Fig. 1 we present relaxed structures of ZZ@ZZ, AC@AC and ZZ@AC double-walled carbon nanotubes (DWCNTs) and double-walled boron nitride nanotubes (DWBNNTs) with outer diameters in the range of 5–20 nm. Here the notation ZZ@AC, for example, represents a DWNT with an inner ZZ tube inside an outer AC shell. The most prominent feature evident in Fig. 1 is that for achiral DWNTs cross-sectional polygonalization occurs when the inner and outer shells share the same chiral angle, whereas for the mixed ZZ@AC systems the cross-section remains circular. Furthermore, both the carbon and BN systems studied exhibit a critical diameters of 5–7 nm and 9–13 nm for the AC@AC and ZZ@ZZ DWNTs, respectively, beyond which faceting appears. This is in remarkable agreement with recent experimental observations that suggest a critical faceting diameter of approximately 12 nm in MWBNNTs[7].

To elucidate the interlayer effects underlying the formation of facets, in Fig. 1 we visualize the degree of local interlayer commensurability by colouring each atom of the outer shell according to the value of its local registry index (LRI, see Methods and Supplementary Section 4 for a detailed explanation). Focusing first on the pre-optimized structures with circular cross-sections (see rows marked

Figure 1 | Relaxed achiral DWNT geometries and LRI patterns. Schematic representation of achiral DWCNTs (top two rows) and DWBNNTs (bottom two rows), showing their structure and local registry patterns before and after geometry relaxation. The pre-optimized structures represent the lowest energy interlayer configuration of each system with a circular cross-section. Optimization has been performed using the Airebo intralayer and Kolmogorov–Crespi interlayer potentials for the DWCNTs and the Tersoff intralayer and h-BN ILP interlayer potentials for the DWBNNTs (see Methods). Each frame includes seven DWNTs with diameters in the range of 5–20 nm. Five groups of DWNTs are presented (from left to right): ZZ@ZZ $(n,0)@(n + 8,0)$; AC@AC $(n,n)@(n + 4,n + 4)$, $(n,n)@(n + 5,n + 5)$ and $(n,n)@(n + 6,n + 6)$; and ZZ@AC. For the ZZ@ZZ systems we choose $n = 55, 80, 105, 130, 155, 180$ and 243. For the AC@AC systems we use $n = 31, 46, 60, 75, 89, 104$ and 140. For the ZZ@AC systems we consider the following set: $(54,0)@(36,36)$, $(80,0)@(51,51)$, $(104,0)@(65,65)$, $(130,0)@(80,80)$, $(154,0)@(94,94)$, $(179,0)@(108,108)$ and $(241,0)@(144,144)$. The LRI colour bar (right) ranges from blue to red, representing the optimal and worst stacking modes of graphene and h-BN, respectively. Grey, pink and blue spheres represent carbon, boron and nitrogen atoms, respectively. These colours should not be confused with the colours used in the LRI patterns for all of the DWNTs in the left panel.

by 'Initial' in Fig. 1) a unique pattern is revealed for the ZZ@ZZ and AC@AC DWNTs where localized out-of-registry areas (marked in red) appear along the circular circumference and are separated by arcs with better registry (white and blue regions). Upon structural relaxation the former develop into vertices whereas the latter form the facets, resulting in an overall improvement of the interlayer registry (see Supplementary Movie 1). Furthermore, the vertices that bear most of the mechanical tension are characterized by a larger interlayer registry mismatch compared with the facets that form almost optimally stacked flat interfaces. Interestingly, along the circumference of the pre-optimized ZZ@AC DWNTs studied a uniform interlayer registry picture appears. Hence, in the absence of a symmetry-breaking driving force acting to promote polygonization, the systems remain circular after optimization and no faceting occurs. A similar picture is found for AC@ZZ systems (see Supplementary Section 2).

An important question that remains unanswered is what dictates the number of facets formed in the AC@AC and ZZ@ZZ systems? Answering this requires the understanding of what determines how many incommensurate regions appear along the circumference of the pre-optimized circular DWNTs. This turns out to be a purely geometric problem that can be readily addressed using the LRI method. To demonstrate this we have considered three sets of AC@AC DWNTs with varying interlayer distances, including the $(n,n)@(n + 4,n + 4)$, $(n,n)@(n + 5,n + 5)$, and $(n,n)@(n + 6,n + 6)$ systems, where the notation $(n,n)@(n + 4,n + 4)$, for example, represents a DWNT with an inner (n,n) shell and an outer $(n + 4,n + 4)$ wall (see Fig. 1). Comparing the pre-optimized registry patterns of the three sets it becomes evident that the number of localized incommensurate regions (and hence the eventual number of vertices found in the final relaxed structures) is given by the difference in the number

of circumferential unit cells between the inner and outer walls regardless of the DWNT diameter. Namely, for the $(n,n)@(n + 4,n + 4)$ system four incommensurate regions form and, similarly, for the $(n,n)@(n + 5,n + 5)$ and $(n,n)@(n + 6,n + 6)$ systems five and six incommensurate regions form, respectively, for all values of the nanotube index, n, considered. Each arc connecting two localized incommensurate regions is a circumferential completion of a one unit cell misfit between the inner and outer layers. Interestingly, the mismatch in the number of circumferential unit cells tends to evenly spread along the circumference of the circular DWNTs even when the walls do not have a mutual rotational symmetry. However, when the inner and outer tube indices share a greatest common divisor (GCD) that is greater than one, the DWNT obtains a GCD-fold rotational symmetry and the registry patterns become fully periodic[18] (for example the $(60,60)@(65,65)$ DWNT has a GCD of $(60,65) = 5$, which also equals the difference in the number of circumferential unit cells between the outer and inner walls and hence the incommensurate regions are of exact five-fold rotational symmetry; on the other hand, the $(31,31)@(36,36)$ system has a GCD of $(31,36) = 1$ and the registry patterns are only nearly periodic). We note that secondary kinks appear between each pair of main vertices upon structural relaxation of all of the AC@AC DWCNTs studied and some of the larger AC@AC DWBNNTs considered, thus doubling the number of facets formed.

Chiral double-walled nanotubes

We now turn to address the more general case of DWNTs that consist of at least one chiral layer. Similar to their achiral counterparts, monochiral DWBNNTs, whose inner and outer walls share the same chiral angle $(\Delta\theta = \theta_{Outer} - \theta_{Inner} = 0°)$, present registry patterns with axial symmetry (see upper left
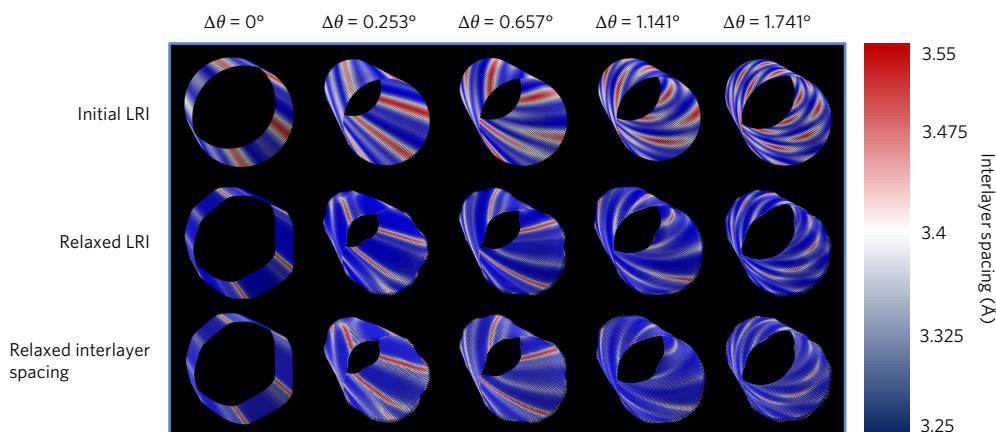
Figure 2 | Relaxed chiral DWBNNT geometries, LRI patterns and interlayer distance. Schematic representation of (120,100)@(126,105) (leftmost column), (60,60)@(66,65) (second column), (70,70)@(77,74) (third column), (68,68)@(75,70) (fourth column) and (71,71)@(80,72) (rightmost column) DWBNNTs showing their local registry patterns before (top row) and after (middle row) geometry relaxation performed using the Tersoff intralayer and h-BN ILP interlayer potentials (see Methods). The colour bar on the right refers to the interlayer spacing of the different systems presented in the bottom row. The colours used in the LRI patterns are the same as in Fig. 1. The chiral angle difference between the inner and outer shells is indicated above each column.

panel of Fig. 2; results for DWCNTs show a very similar behaviour and are presented in Supplementary Section 3). As before, localized incommensurate regions appear along the circumference of the pre-optimized structures. Nevertheless, the (near-) rotational symmetry obtained for the achiral systems is lost and their degree of registry mismatch varies. Here too upon structural relaxation the incommensurate regions thin down and form corners that are separated by axial facets with increased interlayer commensurability (middle left panel). This is more clearly seen in the interlayer distance analysis (lower left panel), where the facets present a nearly optimal (approximately 3.33 Å) interlayer separation, whereas the vertices show an increase of up to 0.2 Å.

The four right columns of Fig. 2 show various bichiral DWBNNTs, whose inner and outer walls differ in their chiral angles ($\Delta\theta \neq 0°$). These systems present non-axial registry patterns that coil around the circumference of the tube with a helical angle that depends on the chiral angle difference between the two walls. For the bichiral DWBNNTs with smaller chiral angle mismatches ($\Delta\theta = 0.253°$ and $0.657°$), long incommensurate stripes appear that are separated by helical almost commensurate arcs (upper panels of the second and third columns). Similar to the monochiral DWBNNT case, upon structural relaxation the incommensurate stripes become thinner and form corners with increased interlayer distances whereas the nearly commensurate arcs turn into helical facets with close-to-optimal interlayer spacing (see the middle and lower panels). This is in fact the most common faceting pattern observed in experiments[2,3,5,6]. For larger chiral angle mismatches (the two rightmost columns) the incommensurate regions become discontinuous (upper panels) resulting in non-faceted optimized structures (middle and lower panels).

Two-dimensional mapping

This complex behaviour can be fully rationalized by the theory of Moiré patterns in planar mismatched hexagonal lattices[19]. To this end, the registry patterns that appear in a DWNT with a circular cross-section are mapped onto the corresponding flat bilayer system. This is achieved by first unrolling the tube shells to obtain two infinite parallel ribbons followed by a contraction of the wider ribbon, representing the outer shell, to match the width of the inner ribbon, thus mimicking curvature effects (see Fig. 3a)[18,19]. The resulting planar bilayer is thus periodic along the circumferential

direction. The obtained Moiré patterns form a super structure whose lattice vectors are given by:

$$
\begin{cases}
\boldsymbol{L}_1^M = \dfrac{\sqrt{3}d\sin(\bar{\theta})}{2(1 + c_h'/c_h)\sin\left(\dfrac{\Delta\theta}{2}\right)} \\[4pt]
\qquad \times \left\{ 2\hat{\boldsymbol{x}} + \left[(1 - c_h'/c_h)\cot\left(\dfrac{\Delta\theta}{2}\right) - (1 + c_h'/c_h)\cot(\bar{\theta}) \right]\hat{\boldsymbol{y}} \right\} \\[8pt]
\boldsymbol{L}_2^M = \dfrac{\sqrt{3}d\sin\left(\bar{\theta} - \dfrac{\pi}{3}\right)}{2(1 + c_h'/c_h)\sin\left(\dfrac{\Delta\theta}{2}\right)} \\[4pt]
\qquad \times \left\{ 2\hat{\boldsymbol{x}} + \left[(1 - c_h'/c_h)\cot\left(\dfrac{\Delta\theta}{2}\right) - (1 + c_h'/c_h)\cot\left(\bar{\theta} - \dfrac{\pi}{3}\right) \right]\hat{\boldsymbol{y}} \right\}
\end{cases}
$$

$$(1)$$

where c_h and c_h' are the chiral vector lengths of the inner and outer NT walls, respectively, $\bar{\theta}$ is the average chiral angle of the two tube walls, $\Delta\theta$ is the corresponding chiral angle difference, d is the nearest-neighbour interatomic distance within each tube wall and $\{\hat{\boldsymbol{x}}, \hat{\boldsymbol{y}}\}$ is the orthogonal reference frame defined by two unit vectors lying along the chiral and translation vector directions of the inner tube wall (a detailed derivation is given in Supplementary Section 7).

For both achiral and monochiral nanotubes $\Delta\theta = 0°$ and the Moiré lattice vectors become parallel to the translational vector of the tube with diverging length, thus resulting in the extended axial LRI patterns appearing both in the curved (Fig. 1 and left column of Fig. 2) and in the planar (Fig. 3c,d) representation of the DWNTs. Upon increasing $\Delta\theta$ the Moiré lattice vectors deviate from the translational vector, thus developing the commonly observed helical patterns along the circumference of the tube (Figs 2 and 3e). Importantly, as the length of the Moiré lattice vectors reduces with increasing $\Delta\theta$ (see Fig. 3b) the density of lattice mismatch regions increases (see the right column of Figs 2 and 3f) thus suppressing the formation of extended facets. This clearly demonstrates that faceting requires matching of the interlayer chiral angle[20]. We note, however, that even in the case of $\Delta\theta = 1.741°$, with $\left|\boldsymbol{L}_1^M\right| = 4.305$ nm and $\left|\boldsymbol{L}_2^M\right| = 17.157$ nm, the optimized structure exhibits interlayer distance variations that correlate with the registry patterns. Notably, similar variations have been recently observed on the surface of CNTs[21,22].
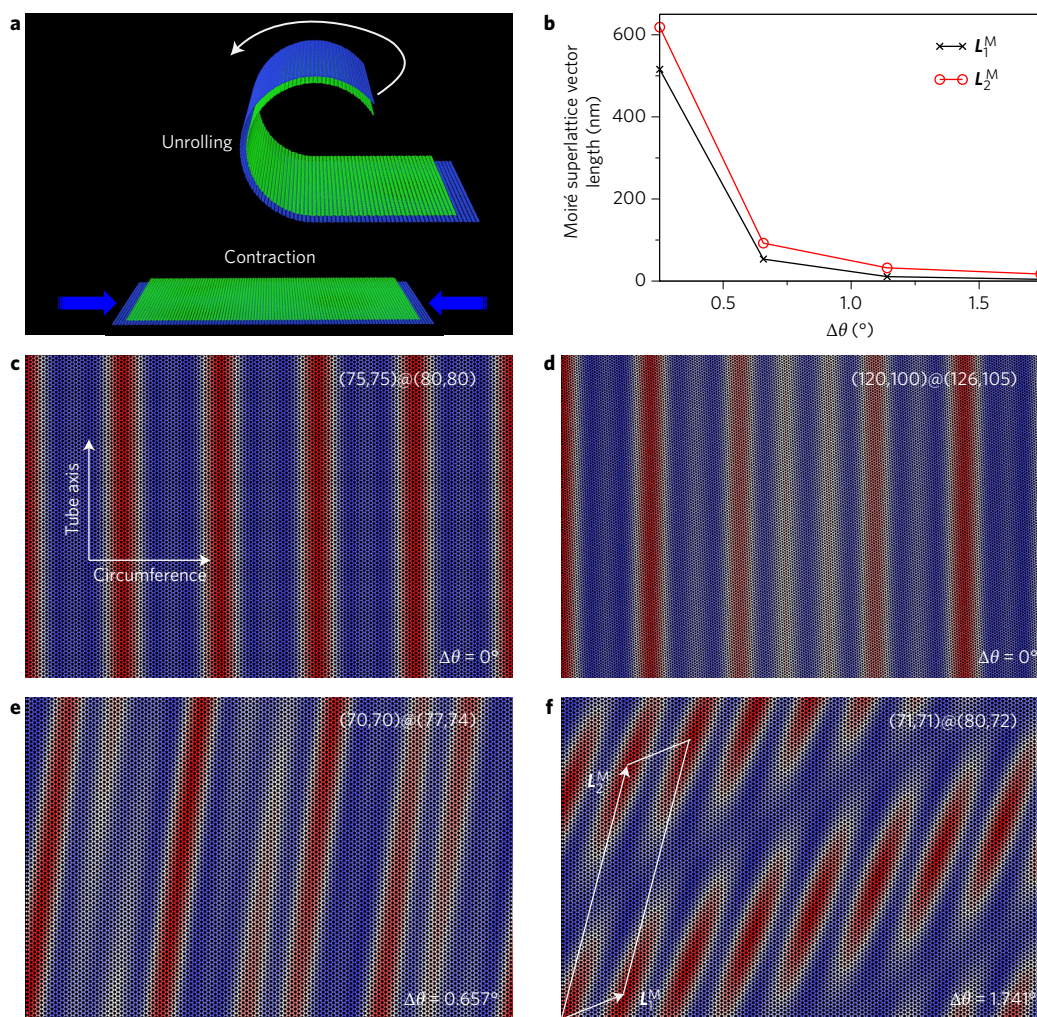
Figure 3 | Planar mapping of DWNT registry patterns. a, Schematic illustration of NT unrolling and compression, resulting in the planar mapping of the DWNT registry patterns. The atoms of the inner and outer walls are coloured green and blue, respectively. **b**, Dependence of the Moiré lattice vector lengths on the chiral angle difference between the DWNT walls as calculated using equation (1). **c,d**, Planar mapping of the registry patterns of the (75,75)@(80,80) and (120,100)@(126,105) DWBNNTs with $\Delta\theta = 0°$ characterized by axial registry patterns. **e,f**, Planar mapping of the helical registry patterns of the (70,70)@(77,74) and (71,71)@(80,72) DWBNNTs with $\Delta\theta = 0.657°$ and $\Delta\theta = 1.741°$, respectively. The Moiré superlattice cell of the (71,71)@(80,72) DWBNNT calculated using equation (1) is represented by the white parallelogram in **f**. The horizontal and vertical axes in **c–f** correspond to the circumferential and axial directions of the DWBNNTs, respectively. The LRI colour bar is the same as in Fig. 1.

Conclusions

To summarize, the origin of MWNT circumferential faceting is found to be a direct consequence of the interlayer lattice registry patterns. The appearance of extended facets requires chiral angle matching between adjacent nanotube layers. For two achiral neighbouring layers of the same type (AC or ZZ) extended axial facets with (almost) perfect rotational symmetry are formed, the number of which is dictated by the corresponding difference in the number of circumferential unit cells. The critical diameter for faceting in these systems is found to be 5–13 nm, in good agreement with experimental findings. Similarly, monochiral layers present extended axial facets but with reduced rotational symmetry. Bichiral adjacent layers exhibit helical facets whose length decreases and helix angle increases as the interlayer chiral angle difference increases up to a point at which facet formation is suppressed, resulting in a corrugated nanotube surface in good agreement with experimental findings. This in turn provides an explanation for why faceting is more abundant in MWBNNTs than in MWCNTs. The polar nature of the heteronuclear BN covalent bonds in MWBNNTs introduces interlayer electrostatic interactions[23] that are sufficient to induce the interwall chiral angle correlation[5,24–26] that is required for the formation of facets. The lack of such interactions in MWCNTs, which are composed of nonpolar homonuclear C–C covalent bonds, often results in practically random chiral angle distributions in the different nanotube layers[21,22,27–34], which may explain why mostly non-faceted structures appear. We note however that low-temperature synthesis conditions have been reported to produce monochiral MWCNTs[27,35]. It is therefore evident that gaining control over interlayer registry matching provides a route for the mechanical enforcement[7] as well as the tuning of tribological[9], electronic[8], and thermal properties of MWNTs[36].

Methods

Methods and any associated references are available in the online version of the paper.

References

1. Liu, M. & Cowley, J. M. Structures of the helical carbon nanotubes. *Carbon* **32**, 393–403 (1994).

2. Gogotsi, Y., Libera, J. A., Kalashnikov, N. & Yoshimura, M. Graphite polyhedral crystals. *Science* **290,** 317–320 (2000).
3. Zhang, G., Jiang, X. & Wang, E. Tubular graphite cones. *Science* **300,** 472–474 (2003).
4. Zhang, G. Y., Bai, X. D., Wang, E. G., Guo, Y. & Guo, W. Monochiral tubular graphite cones formed by radial layer-by-layer growth. *Phys. Rev. B* **71,** 113411 (2005).
5. Celik-Aktas, A., Zuo, J. M., Stubbins, J. F., Tang, C. C. & Bando, Y. Double-helix structure in multiwall boron nitride nanotubes. *Acta Crystallogr. Sect. A* **61,** 533–541 (2005).
6. Golberg, D., Mitome, M., Bando, Y., Tang, C. C. & Zhi, C. Y. Multi-walled boron nitride nanotubes composed of diverse cross-section and helix type shells. *Appl. Phys. A* **88,** 347–352 (2007).
7. Garel, J. *et al.* Ultrahigh torsional stiffness and strength of boron nitride nanotubes. *Nano Lett.* **12,** 6347–6352 (2012).
8. Garel, J. *et al.* BCN nanotubes as highly sensitive torsional electromechanical transducers. *Nano Lett.* **14,** 6132–6137 (2014).
9. Nigues, A., Siria, A., Vincent, P., Poncharal, P. & Bocquet, L. Ultrahigh interlayer friction in multiwalled boron nitride nanotubes. *Nat. Mater.* **13,** 688–693 (2014).
10. Golberg, D. *et al.* Boron nitride nanotubes and nanosheets. *ACS Nano* **4,** 2979–2993 (2010).
11. De Volder, M. F. L., Tawfick, S. H., Baughman, R. H. & Hart, A. J. Carbon nanotubes: present and future commercial applications. *Science* **339,** 535–539 (2013).
12. Arash, B., Wang, Q. & Varadan, V. K. Mechanical properties of carbon nanotube/polymer composites. *Sci. Rep.* **4,** 6479 (2014).
13. Yoon, M., Howe, J., Tibbetts, G., Eres, G. & Zhang, Z. Polygonization and anomalous graphene interlayer spacing of multi-walled carbon nanofibers. *Phys. Rev. B* **75,** 165402 (2007).
14. Golovaty, D. & Talbott, S. Continuum model of polygonization of carbon nanotubes. *Phys. Rev. B* **77,** 081406(R) (2008).
15. Tibbetts, K., Doe, R. & Ceder, G. Polygonal model for layered inorganic nanotubes. *Phys. Rev. B* **80,** 014102 (2009).
16. Mu, W., Zhang, G. & Ou-Yang, Z. Spontaneous polygonization of multiwalled carbon nanotubes: perturbation analysis. *Jpn. J. Appl. Phys.* **51,** 065101 (2012).
17. Palser, A. H. R. Interlayer interactions in graphite and carbon nanotubes. *Phys. Chem. Chem. Phys.* **1,** 4459–4464 (1999).
18. Hod, O. Quantifying the stacking registry matching in layered materials. *Isr. J. Chem.* **50,** 506–514 (2010).
19. Koshino, M., Moon, P. & Son, Y.-W. Incommensurate double-walled carbon nanotubes as one-dimensional moiré crystals. *Phys. Rev. B* **91,** 035405 (2015).
20. Kolmogorov, A. N. & Crespi, V. H. Smoothest bearings: interlayer sliding in multiwalled carbon nanotubes. *Phys. Rev. Lett.* **85,** 4727–4730 (2000).
21. Hashimoto, A. *et al.* Atomic correlation between adjacent graphene layers in double-wall carbon nanotubes. *Phys. Rev. Lett.* **94,** 045504 (2005).
22. Schouteden, K., Volodin, A., Li, Z. & Van Haesendonck, C. Atomically resolved Moiré-type superstructures in double-walled carbon nanotubes. *Carbon* **61,** 379–385 (2013).
23. Hod, O. Graphite and hexagonal boron-nitride have the same interlayer distance. Why? *J. Chem. Theory and Comput.* **8,** 1360–1369 (2012).
24. Golberg, D. *et al.* Fine structure of boron nitride nanotubes produced from carbon nanotubes by a substitution reaction. *J. Appl. Phys.* **86,** 2364–2366 (1999).
25. Golberg, D., Bando, Y., Kurashima, K. & Sato, T. Ropes of BN multi-walled nanotubes. *Solid State Commun.* **116,** 1–6 (2000).
26. Celik-Aktas, A., Zuo, J. M., Stubbins, J. F., Tang, C. & Bando, Y. Structure and chirality distribution of multiwalled boron nitride nanotubes. *Appl. Phys. Lett.* **86,** 133110 (2005).
27. Xu, Z., Bai, X., Wang, Z. L. & Wang, E. Multiwall carbon nanotubes made of monochirality graphite shells. *J. Am. Chem. Soc.* **128,** 1052–1053 (2006).
28. Zuo, J. M., Vartanyants, I., Gao, M., Zhang, R. & Nagahara, L. A. Atomic resolution imaging of a carbon nanotube from diffraction intensities. *Science* **300,** 1419–1421 (2003).
29. Li, F. *et al.* Identification of the constituents of double-walled carbon nanotubes using Raman spectra taken with different laser-excitation energies. *J. Mater. Res.* **18,** 1251–1258 (2003).
30. Koziol, K., Shaffer, M. & Windle, A. Three-dimensional internal order in multiwalled carbon nanotubes grown by chemical vapor deposition. *Adv. Mater.* **17,** 760–763 (2005).
31. Ducati, C. *et al.* Crystallographic order in multi-walled carbon nanotubes synthesized in the presence of nitrogen. *Small* **2,** 774–784 (2006).
32. Hirahara, K. *et al.* Chirality correlation in double-wall carbon nanotubes as studied by electron diffraction. *Phys. Rev. B* **73,** 195420 (2006).
33. Gao, M., Zuo, J. M., Zhang, R. & Nagahara, L. A. Structure determinations of double-wall carbon nanotubes grown by catalytic chemical vapor deposition. *J. Mater. Sci.* **41,** 4382–4388 (2006).
34. Guan, L., Suenaga, K. & Iijima, S. Smallest carbon nanotube assigned with atomic resolution accuracy. *Nano Lett.* **8,** 459–462 (2008).
35. Guo, W. & Guo, Y. Energy optimum chiralities of multiwalled carbon nanotubes. *J. Am. Chem. Soc.* **129,** 2730–2731 (2007).
36. Liu, K. H. *et al.* Van der Waals-coupled electronic states in incommensurate double-walled carbon nanotubes. *Nat. Phys.* **10,** 737–742 (2014).

Acknowledgements

Author contributions

I.L. and R.G. coded the relevant force-fields, performed the geometry optimizations and actively participated in the analysis of the results and the writing of the manuscript. I.L. and O.H. coded the unrolled nanotube registry pattern analysis tool and analysed the corresponding results. E.T., A.V. and O.H. guided the research and data analysis and led the writing of the manuscript.

Additional information

Supplementary information is available in the online version of the paper. Reprints and permissions information is available online at www.nature.com/reprints. Correspondence and requests for materials should be addressed to O.H.

Competing financial interests

The authors declare no competing financial interests.

Methods

Geometry optimization of all DWNTs considered have been performed using quenched dynamics techniques with dedicated intra- and interlayer classical force-fields. For CNTs the intralayer interactions have been described utilizing both the Tersoff[37] potential (see Supplementary Section 1) and the reactive Airebo[38] force-field, adopting the parameterization of ref. 39. The interlayer interactions of these systems have been described by the registry dependent Kolmogorov–Crespi[40] potential. For the intralayer interactions of BNNTS we have used the Tersoff[41] force-field as parameterized in ref. 41 for BN-based systems along with our recently developed h-BN interlayer potential (h-BN ILP) with frozen partial charges (see Supplementary Section 5)[42]. Cyclic boundary conditions have been applied for all achiral and monochiral (bearing the same chirality) DWNTs. We further verify the robustness of our results towards potential many-body dispersion effects that have been neglected in the parameterization procedure of the h-BN ILP (see Supplementary Section 6).

For the registry analysis we have extended the global registry index (GRI) method, which quantifies the interlayer stacking registry in rigid layered materials[18,43–45], by defining the local registry index that characterizes the local degree of lattice commensurability in various regions along the circumference of the nanotube. In short, in the original GRI approach a single parameter is calculated as the sums and differences of all of the projected atomic-centred circle overlaps between adjacent layers to characterize the overall registry matching of the system at a given interlayer configuration. In the LRI approach each atomic centre is assigned a number that indicates the local degree of registry in its immediate surrounding environment. This is achieved by calculating the projected overlaps between the circles (or Gaussians) assigned to a given atom and one of its nearest neighbours in one layer and all of the circles (Gaussians) of its adjacent layer using the same system-dependent circle radii (Gaussian standard deviation), formula and normalization as in the GRI approach. This procedure is repeated for all of the

nearest neighbours of the given atom and the average result is assigned to this atom as its LRI, such that a value of 0 marks good local registry (lowest interlayer energy) and 1 represents bad local registry (highest interlayer energy). The LRI map is then obtained by plotting one of the NT layers and using a colour scheme in which an atom with the highest LRI value of 1 is coloured in red and an atom having the lowest LRI value (0) is coloured in blue (see Figs 1–3). For further details see Supplementary Section 4.

References

37. Tersoff, J. Modeling solid-state chemistry—interatomic potentials for multicomponent systems. *Phys. Rev. B* **39,** 5566–5568 (1989).
38. Stuart, S. J., Tutein, A. B. & Harrison, J. A. A reactive potential for hydrocarbons with intermolecular interactions. *J. Chem. Phys.* **112,** 6472 (2000).
39. Lindsay, L. & Broido, D. A. Optimized Tersoff and Brenner empirical potential parameters for lattice dynamics and phonon thermal transport in carbon nanotubes and graphene. *Phys. Rev. B* **81,** 205441 (2010).
40. Kolmogorov, A. N. & Crespi, V. H. Registry-dependent interlayer potential for graphitic systems. *Phys. Rev. B* **71,** 235415 (2005).
41. Sevik, C., Kinaci, A., Haskins, J. B. & Çağın, T. Characterization of thermal transport in low-dimensional boron nitride nanostructures. *Phys. Rev. B* **84,** 085409 (2011).
42. Leven, I., Azuri, I., Kronik, L. & Hod, O. Inter-layer potential for hexagonal boron nitride. *J. Chem. Phys.* **140,** 104106 (2014).
43. Marom, N. *et al.* Stacking and registry effects in layered materials: the case of hexagonal boron nitride. *Phys. Rev. Lett.* **105,** 046801 (2010).
44. Hod, O. Interlayer commensurability and superlubricity in rigid layered materials. *Phys. Rev. B* **86,** 075444 (2012).
45. Hod, O. The registry index: a quantitative measure of materials' interfacial commensurability. *ChemPhysChem* **14,** 2376–2391 (2013).